ELSEVIER

BIOMATERIALS ADVANCES

materialstoday

Check for updates

Multifunctional targeted solid lipid nanoparticles for combined photothermal therapy and chemotherapy of breast cancer

Andreia Granja [a], Rita Lima-Sousa [b], Cátia G. Alves [b], Duarte de Melo-Diogo [b], Cláudia Nunes [a], Célia T. Sousa [c,d], Ilídio J. Correia [b,e,*], Salette Reis [a,*]

[a] LAQV, REQUIMTE, Departamento de Ciências Químicas, Faculdade de Farmácia, Universidade do Porto, 4050-313 Porto, Portugal
[b] CICS-UBI – Centro de Investigação em Ciências da Saúde, Universidade da Beira Interior, 6200-506 Covilhã, Portugal
[c] IFIMUP and Departamento de Física e Astronomia da Faculdade de Ciências da Universidade do Porto, Rua do Campo Alegre 687, 4169-007 Porto, Portugal
[d] Departamento de Física Aplicada, Facultad de Ciencias, Universidad Autónoma de Madrid (UAM), Campus de Cantoblanco, C/ Francisco Tomás y Valiente, 7, M 12 604 - 28049 Madrid, Spain
[e] CIEPQPF – Departamento de Engenharia Química, Universidade de Coimbra, Rua Sílvio Lima, 3030-790 Coimbra, Portugal

ARTICLE INFO

ABSTRACT

Photothermal therapy has emerged as a new promising strategy for the management of cancer, either alone or combined with other therapeutics, such as chemotherapy. The use of nanoparticles for multimodal therapy can improve treatment performance and reduce drug doses and associated side effects. Here we propose the development of a novel multifunctional nanosystem based on solid lipid nanoparticles co-loaded with gold nanorods and mitoxantrone and functionalized with folic acid for dual photothermal therapy and chemotherapy of breast cancer. Nanoparticles were produced using an economically affordable method and presented suitable physicochemical properties for tumor passive accumulation. Upon Near-Infrared irradiation (808 nm, 1.7 W cm^{-2}, 5 min), nanoparticles could effectively mediate a temperature increase of >20 °C. Moreover, exposure to light resulted in an enhanced release of Mitoxantrone. Furthermore, nanoparticles were non-hemolytic and well tolerated by healthy cells even at high concentrations. The active targeting strategy was found to be successful, as shown by the greater accumulation of the functionalized nanoparticles in MCF-7 cells. Finally, the combined effects of chemotherapy, light-induced drug release and photothermal therapy significantly enhanced breast cancer cell death. Overall, these results demonstrate that the developed lipid nanosystem is an efficient vehicle for breast cancer multimodal therapy.

1. Introduction

Breast cancer is the main cause of cancer-related deaths in women globally [1] Given the high complexity and heterogeneity of the disease, the standard breast cancer treatment regimens generally encompass multidrug and multimodal therapy [2,3]. However, the majority of these therapeutics are non-specific, which leads to off-target systemic toxicity and reduced efficacy [4]. To surpass some of these limitations, new treatment modalities for breast cancer management such as photothermal therapy (PTT) have emerged. PTT is a safe, minimally invasive, and precise procedure based on the delivery of a photoabsorbing agent to the tumor region, followed by light irradiation, generally in the Near-Infrared region (NIR; 750–1000 nm). The photothermal agent converts the light energy into heat, which can directly elicit cancer cell death and

when combined with other modalities such as chemotherapy, improve its therapeutic effect [5]. Gold nanostructures, such as gold nanorods (AuNRs) are considered excellent photothermal agents given their high biocompatibility and versatility, along with a high light-to-heat conversion efficiency [6].Thus, they have been explored as photothermal agents for breast cancer therapy, either alone or in combination with other therapeutics [7–10]. The development of a multifunctional nanosystem comprising PTT and chemotherapy represents a promising therapeutic strategy, as the combined actions of the two modalities can result in higher anti-cancer efficacy, drug dosages reduction, and multidrug resistance limitation [11–13]. In addition, the incorporation of the two modalities into one single nanoplatform opens the possibility for the development of smart nanosystems, which can release their cargo upon NIR light irradiation, further improving the performance and

selectivity of the treatment [14]. Different nanoplatforms co-loaded with AuNRs and chemotherapeutics have already been reported including liposomes [15,16], dendrimers [17] mesoporous silica [18,19], albumin [20] and polymeric [21] nanoparticles. Lipid nanoparticles represent a simple, biocompatible, economically affordable, and versatile type of nanocarrier, which can be explored for the design of multifunctional nanosystems [22,23]. Up to this date, only one study combining drug delivery and gold nanostructures for dual PTT and chemotherapy using lipid nanoparticles has been reported [24]. Zheng et al. produced nanostructured lipid carriers (NLC) decorated with polyethylene glycol (PEG) and hyaluronic acid and loaded with doxorubicin and polyhedral gold nanoparticles, presenting encouraging results [24]. To the best of our knowledge AuNRs-loaded solid lipid nanoparticles (SLN) for PTT has not been reported. Recently, we have designed SLN using a cost-effective organic solvent-free method for the loading of the anti-cancer drug Mitoxantrone (Mito) [25]. Mito is an anthracenedione with high efficacy against different types of cancers, including breast cancer [26]. In addition, Mito has demonstrated enhanced cytotoxicity when combined with hyperthermia *in vitro* [27]. Thus, it may benefit from the combination with AuNRs-mediated PTT. Therefore, here we propose the development of a multifunctional SLN nanoformulation loaded with Mito and AuNRs to take advantage of the combinatory effects of PTT and chemotherapy. Moreover, to improve tumor accumulation and target the folate receptors, which are overexpressed in cancer cells [28], SLN were decorated with a FA conjugate. Nanoparticles were prepared and their main physicochemical characteristics were studied. Additionally, their photothermal capacity and drug release profile upon NIR light irradiation (808 nm, 1.7 W cm^{-2}, 5 min) were evaluated. After that, the hemocompatibility and cytocompatibility of the nanosystem were determined and the targeting efficiency towards MCF-7 cells was studied. Finally, the combination of chemotherapy and PTT was assessed in MCF-7 cells.

2. Materials and methods

2.1. Materials

Coumarin-6 (C6), (98 %), Dicyclohexylcarbodiimide (DCC), Dimethyl sulfoxide, Dulbecco's modified Eagle's medium F-12 (DMEM-F12), Dulbecco's Phosphate Buffered Saline (PBS), Folic acid (FA), Formalin solution, Mitoxantrone hydrochloride (Mito), *N*-hydroxysuccinimide, Penicillin/Streptomycin, Propidium iodide solution, Resazurin, Trimethylamine, Triton™ X-100, Trypan blue solution, Trypsin, Tween® 80 were acquired from Sigma-Aldrich® (St Louis, MO, USA). Lysotracker™ Green and Hoechst 33342® were acquired from Invitrogen, Thermo Fisher Scientific (MA, USA). Fetal Bovine Serum (FBS) was acquired from Biochrom AG (Berlin, Germany). Cetyl Palmitate was provided by Gatefossé (Nanterre, France). Sodium chloride was obtained from Honeywell Fluka™ (NJ, USA). DSPE-PEG$_{2000}$-NH$_2$ (1,2-distearoyl-sn-glycero-3-phosphoethanolamine-N-[amino(polyethylene glycol)-2000] was acquired from Avanti® Polar Lipids Inc. (Alabama, USA). Organic-coated gold nanorods (AuNRs, 10x41nm) were obtained from Nanopartz (Loveland, CO, USA). MCF-7 cell line was acquired from ATCC (Middlesex, UK). Normal Human Dermal Fibroblasts (NHDF) were obtained from Promocell (Heidelberg, Germany).

2.2. Preparation of solid lipid nanoparticles

SLNs were produced by the hot ultra-sonication technique, as reported earlier, with some adaptations [25]. Briefly, solid lipid cetyl palmitate (20 mg) and surfactant Tween® 80 (17.5 mg) were placed in a water bath (70 °C) until the complete melting of the lipid. The production of AuNRs-loaded SLN was carried out by adding a solution of AuNRs (containing 1.6 mg) to the lipid melt. Functionalization of the SLN was performed by adding the FA conjugate (DSPE-PEG$_{2000}$-FA), synthesized as previously reported in our group [29], to the lipid phase

at a ratio of 1 % of the mass of lipid+surfactant. After that, 1.1 mL of pre-warmed PBS buffer (pH 8.2) was added to the lipid melt, sonicated for 5 min (VCX130, Sonics and Materials, 115 Newtown, USA) at 70 % and let to cool to room temperature. For the production of nanoparticles loaded with Mito used for the drug release, cytocompatibility, efficacy and confocal microscopy assays, a drug solution in PBS buffer (470 μg/mL) was previously prepared and poured into the lipid melt prior to the ultrasonication step. To perform the flow cytometry studies, C6-loaded SLN were prepared by solubilizing C6 in the lipid melt at a ratio of 0.025 % of the mass of lipid prior to the addition of the water phase.

2.3. Size, polydispersity index and surface charge measurements

The mean hydrodynamic diameter, polydispersity index (PDI) and surface charge of the nanoparticles were measured using a ZetaPALS analyzer (Brookhaven Instruments Corporation, NY, USA). Nanoformulations were previously diluted in PBS (1:200) and determinations were performed at 20 °C at a scattering angle of 90°. Particle size was also evaluated by nanoparticle tracking analysis (NTA) using a NanoSight NS300 (Malvern Instruments, Worcestershire, UK, CMOS camera, 488 nm laser). Each sample was diluted in distilled water (1:50,000), injected in the viewing chamber at an infusion rate of 50 and measured under constant flow at 24 °C. For each size determination, 5 videos of 20 s were obtained using a detection threshold of 5 and a camera level of 10. The NTA 3.4 software was used to perform data analysis.

2.4. Entrapment efficiency determination

The entrapment efficiency (EE%) was measured indirectly, by quantifying the amount of non-entrapped Mito [25]. With that purpose, SLN (diluted at 1:30 in PBS pH 8.2) were transferred to 50 kDa centrifugal filter devices (Amicon® Ultra Centrifugal Filters, Merck Millipore, Darmstadt, Germany) followed by centrifugation at 2851 × *g* until the total recovery of the aqueous phase. The concentration of free Mito in the supernatant was determined by measuring the absorbance at 610 nm in a Jasco V-660 spectrophotometer (Jasco Corporation, USA). Prior to this assay, a standard curve in PBS pH 8.2 was obtained to determine the concentration of Mito.

The calculation of the drug EE% was performed as follows:

$$EE\% = \frac{\text{Total amount of Mito} - \text{Non-entrapped Mito}}{\text{Total amount of Mito}} \times 100 \quad (1)$$

The loading capacity (LC%) was determined according to the following equation:

$$LC\% = \frac{EE\% \times \text{Total amount of Mito}}{\text{Total amount of lipid}} \times 100 \quad (2)$$

2.5. Heat stability of Mito

Prior to the PTT studies, a heat stability study of Mito was conducted using Nuclear magnetic resonance (NMR) using 3-(trimethylsilyl)propionic-2,2,3,3-d4 acid sodium salt (TSP) as internal standard (δ = 0 ppm). The drug was dissolved in D$_2$O (0.05 % TSP) in an NMR tube and incubated for 30 min at 20, 30, 40, 50, 60 and 70 °C in an NMR spectrometer (Bruker Avance III 400, operating at 400.15 MHz). NMR spectra were recorded and analyzed for each temperature using the standard Bruker software (version 4.01) applying exponential multiplication and Fourier transform and phase correction. Line broadening of 0.30 Hz was used. Each spectrum was analyzed, regarding the potential formation of new signals and the variation of the chemical shifts of the protons of the drug.

2.6. Photothermal capacity evaluation and NIR-induced drug release

To evaluate the photothermal capacity of the AuNRs-loaded SLN,

each sample (200 µL, 24 and 32 µg/mL of AuNRs) was irradiated with a NIR laser (808 nm, 1.7 W cm^{-2}) for 5 min and the temperature variation was measured using a thermocouple thermometer [30]. The Specific Absorption Rate (SAR) and the photothermal conversion efficiency of the nanosystems were then calculated (detailed information regarding the calculations is presented in the Supplementary data).

The *in vitro* drug release was performed with and without NIR laser irradiation using the dialysis method. Briefly, 500 uL of each nano-formulation was placed in the upper unit of a Slide-A-Lyzer™ MINI Dialysis Device (10 kDa, Thermo Scientific™, MA, USA) and immersed into 14 mL of PBS buffer. Dialysis devices were then placed at 37 °C under stirring for 24 h. At specific time-points, 1 mL of each sample was removed from the external media and replaced with 1 mL of pre-heated PBS. For the irradiated samples, nanoformulations were irradiated with the NIR laser (808 nm, 1.7 W cm^{-2}) for 5 min. The amount of drug released at each time-point was quantified by UV–Vis spectrophotometry at 610 nm in an Evolution 201 spectrophotometer (Thermo Scientific™, MA, USA). The release data obtained are presented as mean ± standard deviation.

2.7. Hemolysis assay

To perform the hemolysis assay blood samples were collected from human healthy volunteers by Serviço de Hematologia from Centro Hospitalar Universitário do Porto and stored in ethylenediamine tetra-acetic acid (EDTA)-coated tubes. Blood samples were then centrifuged (955 $\times$ g, 5 min at 4 °C) followed by 3 washing steps with a 0.85 % (*w/v*) saline solution. A 4 % (*v/v*) solution of RBCs was then prepared and incubated with the nanoformulations (diluted in saline solution at the desired concentrations) at a ratio of 1:1 in a 96-well plate at 37 °C. Positive and negative controls consisted of Triton X-100 (1 % v/v) and saline solution, respectively. After 1 h, supernatants were recovered and the absorbance of hemoglobin was measured at 415 nm in a microplate reader (Biotek Instruments, Winooski, VT, USA). Data were obtained using the average of three assays with blood collected from three different donors. The percentage of hemolysis was determined as follows:

$$\text{hemolysis\%} = \frac{\text{Abs(sample)} - \text{Abs(negative control)}}{\text{Abs(positive control)} - \text{Abs(negative control)}} \times 100 \qquad (3)$$

2.8. Cytocompatibility assessment

The cytocompatibility of the lipid nanoformulations was evaluated in normal cells (NHDF) and breast cancer cells (MCF-7) by the resazurin assay, as reported earlier [31]. Cells were seeded in 96-well plates (1 $\times$ 10^4 cells per well) in DMEM-F12 with 10 % (*v/v*) FBS and 1 % (*v/v*) penicillin/streptomycin and were kept at 37 °C, 5 % CO$_2$. After 24 h, cells were incubated with different concentrations of the nano-formulation for 24 h and 48 h. A negative control containing cells incubated with DMEM-F12 was also included. At the end of the incubation, the medium was removed and a resazurin solution (10 % v/v in culture media) was added and incubated for 4 h in dark conditions at 37 °C, 5 % CO$_2$. The fluorescence of the resultant resorufin ($\lambda_{ex}/\lambda_{em}$ of 560/590 nm) was then quantified in a Spectramax Gemini EM spectrofluorometer (Molecular Devices LLC, California, USA).

2.9. Cellular uptake studies

2.9.1. Flow cytometry

Flow cytometry analyses were performed according to earlier protocols described in our group [32]. Briefly, MCF-7 cells were seeded in 24-well plates (2 $\times$ 10^5 cells per well) and incubated for 24 h. After that, C6-marked SLN (250 µg/mL of lipid, with and without the DSPE-PEG$_{2000}$-FA conjugate) were incubated with the cells for specific time points at 37 °C, 5 % CO$_2$. A negative control comprising cells incubated

with DMEM was also included. After each incubation time-point, cells were rinsed two times with PBS, recovered from each well using trypsin, resuspended in PBS and analyzed in a BD Accuri™ C6 flow cytometer (BD Biosciences, Belgium). Staining with PI (0.01 mg/mL) and trypan blue (0.004 %) was performed to eliminate the signal from dead cells and quench the fluorescence from non-internalized nanoparticles. For each condition, 10,000 events were collected. Data analysis was carried out using the BD Accuri™ C6 software (BD Biosciences, Belgium). Graphpad (GraphPad Software Inc., CA, USA) was used to fit the kinetics of time of the cellular uptake to the Michaelis-Menten equation:

$$V = \frac{V_{max} \times t}{k + t} \qquad (4)$$

where V is the cellular uptake in real time V$_{max}$ is the value of saturated cellular uptake, *t* is the incubation time, and k is the time of half maximum uptake.

2.9.2. Confocal microscopy

For confocal laser scanning microscopy (CLSM) imaging, MCF-7 cells (1 $\times$ 10^4 cells per well) were seeded in µ-slide 8-well imaging plates (Ibitreat, Ibidi GmbH, Munich, Germany) and maintained at 37 °C, 5 % CO$_2$. After 24 h, the different nanoformulations (5 µg/mL of lipid) were incubated for 4 h and 24 h. Subsequently, cells were rinsed with PBS three times and 60 nM of Lysotracker™ Green and incubated for 30 min at 37 °C. After washing three times with PBS, cell fixation was carried out using formalin solution incubated for 30 min. After rinsing three times with PBS, nuclei were stained with 8 µM of Hoechst 33342® for 10 min in the dark and, finally, rinsed three times with PBS. CLSM images were obtained using a Leica Stellaris 8 inverted confocal microscope using a 63×/1.4 oil objective and a resolution of 1024 $\times$ 1024 (Leica Microsystems, Wetzlar, Germany). The following excitation/emission wavelengths were used: 405/461 nm for Hoechst 33342®, 504/511 nm for LysoTracker™ Green and 610/630 nm for Mito. Image data were processed using Fiji ImageJ software.

Time-lapse live cell imaging of SLN uptake was also performed using CLSM. MCF-7 cells were seeded on 35 mm µ-Dishes (polymer coated, Ibidi GmbH, Munich, Germany) at a density of 3.6 $\times$ 10^4 cells per dish for 24 h. Cell culture dishes were then placed on the confocal incubator chamber, at 37 °C, 5 % CO$_2$ and nanoformulations (5 µg/mL of lipid) were added and immediately observed in CLSM. Images were automatically collected for up to 30 min with a time interval of 5 min between frames in similar conditions as reported above, except for the channel of LysoTracker™ Green, which was not used.

2.10. Combined chemo and photothermal therapy effects in vitro

The combinatorial effects of chemotherapy and PTT mediated by the nanoparticles were evaluated in MCF-7 cells using the resazurin assay, as reported previously [31]. Briefly, cells were grown in 96-well plates (1 $\times$ 10^4 cells per well) for 24 h at 37 °C, 5 % CO$_2$, and incubated with the different nanoformulations at an equivalent concentration of 24 and 32 µg/mL of AuNRs. After 4 h, cells were irradiated with a NIR laser (808 nm, 1.7 W cm^{-2}) for 5 min. Cells incubated with only DMEM-F12 with and without NIR irradiation were used as a control. Cell viability was then evaluated 24 h after nanoparticle incubation, as described in Section 2.8.

2.11. Statistical analysis

Graphpad Prism6 Software (CA, USA) was used to perform the statistical analysis. Statistical comparisons of the mean between groups were assessed by two-way ANOVA. Differences were considered significant with a *p*-value under 0.05. Data are represented as mean ± SD.

3. Results

3.1. Physicochemical characterization

Two different SLN nanoformulations were produced by the hot ultra-sonication technique. Formulations appeared milky and homogeneous with light brown color due to the loading of AuNRs. After Mito entrapment, the color changed to dark blue. Their main physicochemical characteristics are summarized in Fig. 1. The hydrodynamic size was 206 nm and 212 nm, for SLN Au-FA and SLN Au-Mito-FA, respectively, as measured by DLS. Measurements obtained through NTA, however, showed a relatively smaller particle size of 174 nm and 162 nm, respectively. The differences obtained with the two techniques are related to the ability of NTA to track each nanoparticle individually, while DLS determinations can be biased by the presence of agglomerated particles, as previously highlighted [25]. In general, the results obtained for particle size suggest that the nanoparticles are suitable for intravenous administration and passive tumor targeting [33,34]. PDI was below 0.2, confirming the presence of a monodisperse population for lipid-based nanoparticles [35], which is also corroborated by the particle size distribution graphs obtained through NTA. The low values of zeta potential of approximately -10 mV may be related to the ionic strength of the solvent (PBS), which is much higher than double deionized water [36]. This can be beneficial, since particles with slightly negative surface charges have been shown to more easily accumulate in the tumor region while having limited uptake in normal organs such as the liver [37]. Loading of Mito was efficient, as shown by the EE% of 88 % and LC% of 2.3 % obtained for this nanoformulation. Prior to the PTT, the heat stability of Mito was evaluated through NMR which confirmed that no structural changes occurred in the molecule for temperatures up to 70 °C, suggesting that Mito is suitable for the subsequent studies of PTT (Fig. S1).

3.2. Photothermal effect and NIR-induced drug release

The temperature variation achieved upon NIR light exposure was addressed at two different concentrations of AuNRs (Fig. 2A). At the lowest concentration tested (24 μg/mL) temperature was elevated >20 °C, while at 32 μg/mL an elevation of 25 °C was observed. No differences were found between drug-loaded and unloaded nano-formulations, which suggests that drug loading did not influence the light-to-heat conversion efficiency of the nanosystem. PBS buffer, the solvent used for the production of the SLN, was used as a control, demonstrating only a very limited temperature variation of approximately 2 °C. Additionally, the SAR and the photothermal conversion efficiency were calculated. For both AuNRs concentrations (24 and 32 μg/mL) the obtained SAR value was 1.6×10^4 W/g$_{Au}$ which is in accordance with the results previously reported [38,39]. The photothermal conversion efficiency was found to be 29.4 %, which is in agreement with previous studies using gold nanorods [40,41]. Overall, these data demonstrate that the developed nanosystem is effective for a PTT application at the two concentrations tested.

The release of Mito was investigated in physiological PBS with 5 min of NIR irradiation and without irradiation (Fig. 2B). As shown in Fig. 2B, a controlled release was obtained at the first 6 h of the study, with only 22 % of Mito released to the external media. After NIR irradiation, a higher release of Mito occurred (28 %). This difference between irradiated and non-irradiated samples increased over time. At the end of the assay after 48 h, 76 % of Mito was released, in contrast to the 68 % released from the non-irradiated SLN. These data suggest that the temperature increase occurring following NIR irradiation led to the partial melting of the lipid matrix of the SLN, thus enhancing the release of the drug. Therefore, a higher cancer cell death may be predicted from the combined effects of hyperthermia and enhanced drug release.

3.3. Hemolysis

To assess the suitability of the nanoformulations for intravenous injection, a hemolysis assay was conducted using human blood. Nano-formulations were tested at a concentration range of 8 to 40 μg/mL of AuNRs (corresponding to 97 to 485 μg/mL of lipid). As shown in Fig. 3, nanoparticles induced <1 % hemolysis, even at the highest lipid concentration (Fig. 3A and B). Therefore, according to ISO/TR 7406, those are considered safe for intravenous administration. These results demonstrate that the range of concentration of AuNRs found to be suitable for PTT applications is non-hemolytic.
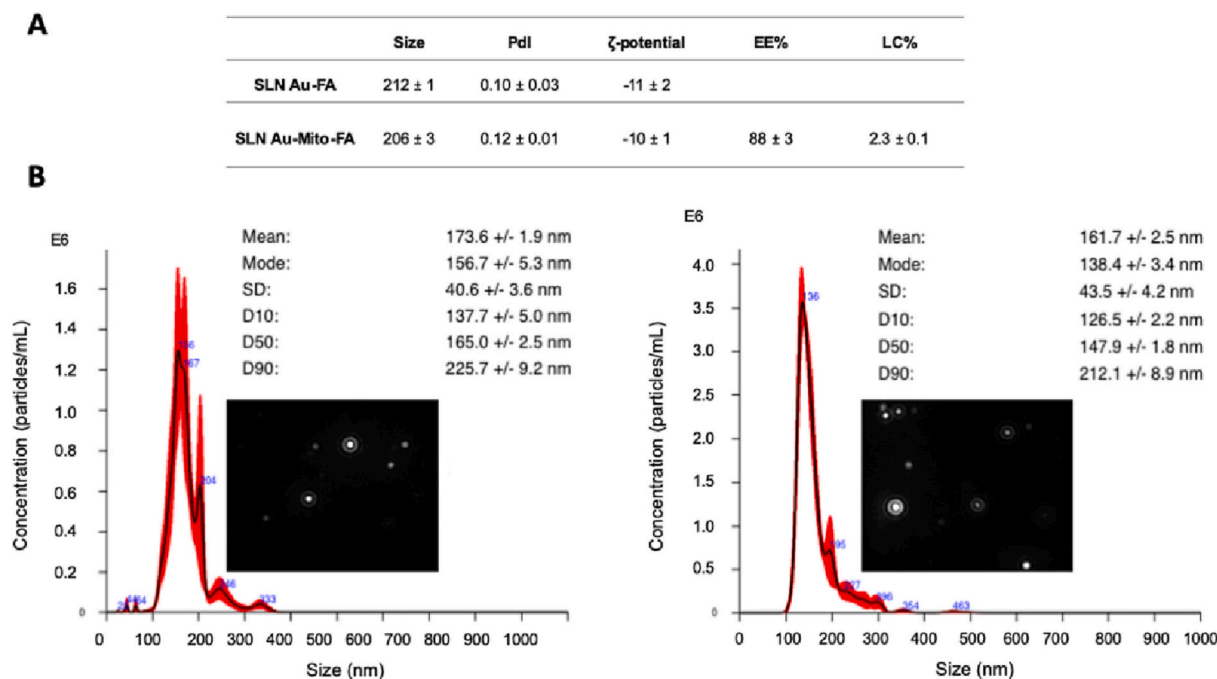

Fig. 1. Physicochemical characterization of SLN Au-Mito-FA and SLN Au-FA. (A) Hydrodynamic size, PDI and zeta potential determined by DLS, EE% and LC%. (B) Particle size distribution measured through NTA and corresponding video frames of SLN Au-FA (left) and SLN Au-Mito-FA (right).
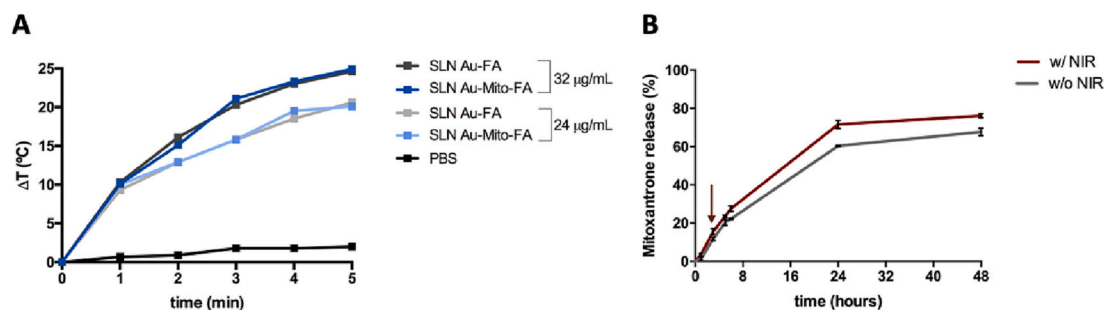
Fig. 2. NIR light irradiation effect on the temperature variation (ΔT) and drug release of the nanoformulations (A) ΔT of SLN Au-FA and SLN Au-FA-Mito at two different concentrations of AuNRs upon irradiation with NIR laser (808 nm, 1.7 W cm^{-2}) for 5 min. PBS was used as a control. (B) Cumulative release of Mito from SLN Au-Mito-FA at 37 °C with and without NIR laser irradiation for 5 min (irradiation was performed 4 h after the starting of the assay). Data are expressed as mean ± SD (*n* = 3). Arrow indicates the time-point of NIR laser irradiation.
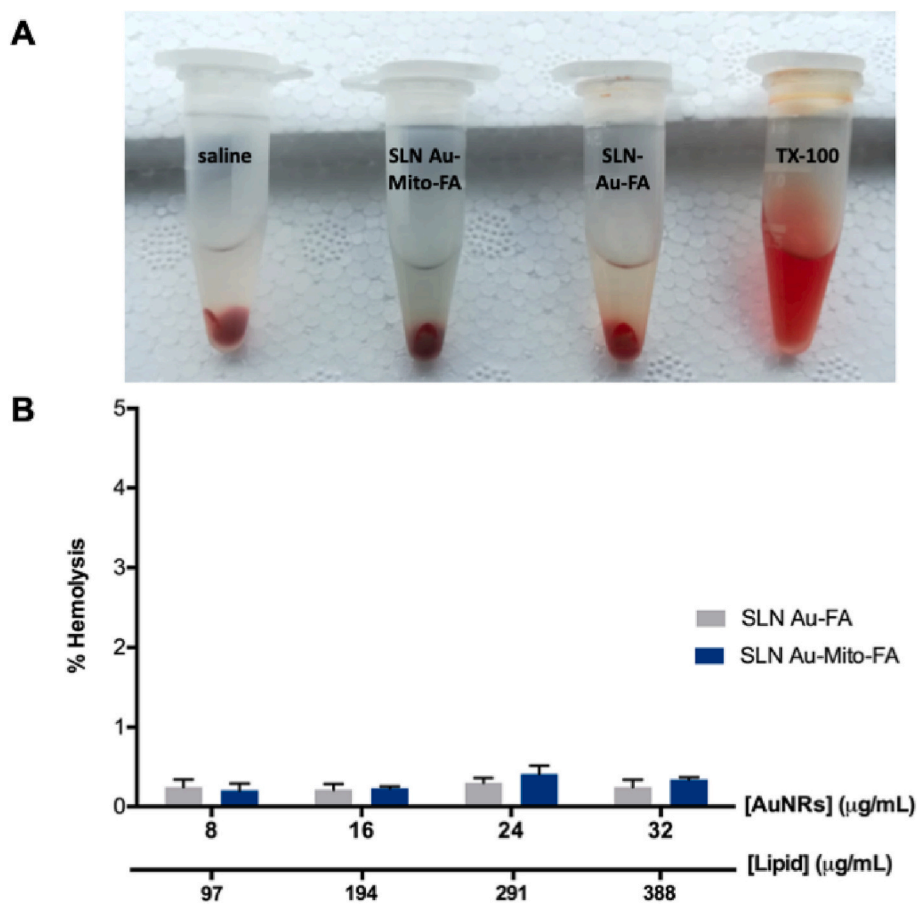
Fig. 3. Hemolysis assay (A) Representative image of human red blood cells treated with the highest concentration of SLN Au-Mito-FA and SLN Au-FA and controls - negative (saline solution) and positive (TX-100 - 1 % *v*/v) after 1 h incubation. (B) Hemolytic activity of the nanoformulations at different concentrations. Data represent the average of three assays using RBCs from three human donors.

3.4. Cytocompatibility assessment

The cytocompatibility of the drug-unloaded nanoparticles (SLN-Au-FA) was also evaluated in normal cells (NHDF) and breast cancer cells (MCF-7) following incubation for 24 and 48 h, as depicted in Fig. 4. The nanoparticles were found to be well tolerated by NHDF up to concentrations of 388 μg/mL of lipid. The same trend was observed for MCF-7 cells following incubation for 24 h. After incubation for 48 h, however, the two highest concentrations (291 μg/mL and 388 μg/mL) induced a reduction in MCF-7 cell viability. These results are in agreement with previous works with similar types of nanoparticles, where NHDF were

found to have high tolerability at a similar or higher range of SLN concentrations [42,43], while MCF-7, presented lower tolerability with values of IC$_{50}$ ranging from 175 μg/mL to 560 μg/mL of SLN after 48 h incubation [44,45]. Moreover, due to the FA active targeting, a higher internalization is prone to occur in MCF-7 cells, which overexpress the FR, in opposite to NHDF [46,47].

3.5. Cellular uptake

The effect of the functionalization on breast cancer cell targeting ability was evaluated by analyzing MCF-7 cellular uptake by flow
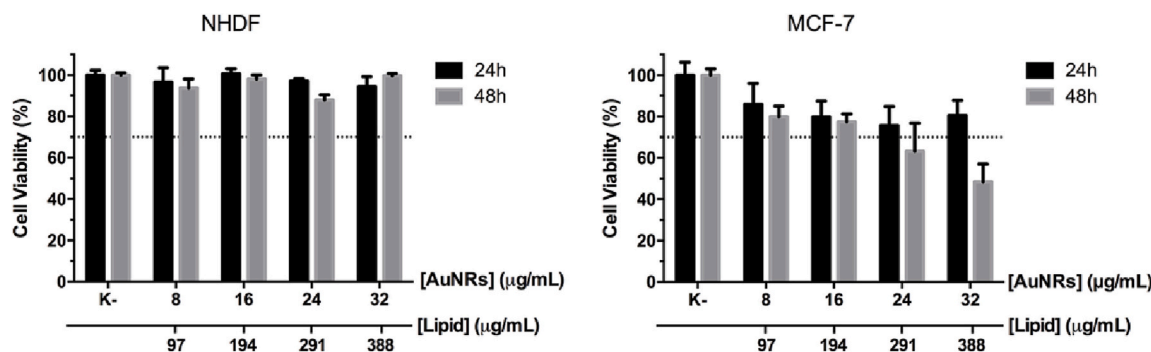
Fig. 4. Cytocompatibility of unloaded SLN. Cell viability was evaluated following incubation with SLN Au-FA at different concentrations in normal (NHDF) and breast cancer cells (MCF-7) after 24 h and 48 h incubation. Data are expressed as mean $\pm$ SD ($n = 5$).

cytometry and CLSM.

For the flow cytometry studies, C6-labelled SLN with and without the DSPE-PEG-FA conjugate (SLN C6-FA and SLN C6) were produced. Nanoparticles were then characterized to confirm that their main properties were not considerably affected, which was demonstrated, with particle sizes of 212 and 230 nm, PDI of 0.11 and 0.06 and zeta potentials of -8 mV and -10 mV, respectively (Table S1). After that, nanoparticles were incubated with MCF-7 cells for different incubation periods up to 24 h. The time-dependent cellular uptake is depicted in Fig. 5A. After incubation with the two types of SLN, a rapid internalization occurred during the first 4 h, followed by a plateau. Moreover, a significantly higher cellular uptake was obtained for SLN C6-FA for all of the studied time points, thus confirming the efficacy of the active

targeting strategy. Additionally, the cellular uptake was found to follow Michaelis-Menten kinetics (Fig. 5B). SLN C6-FA exhibited a 1.3-fold higher saturated cellular uptake (V_{max}) than SLN C6 and a 1.2-fold lower k value, suggesting a higher and quicker cellular internalization, compared to the non-functionalized SLN.

Cellular uptake was also visualized by CLSM. MCF-7 cells were incubated with the nanoformulations for 4 and 24 h. The CLSM images are presented in Fig. 6. After incubation for 4 h, it is possible to observe a high red fluorescence in the cytoplasm of the cells, including in the endosomes and lysosomes, as suggested by the co-localization of the green channel (Lysotracker) and the red channel (Mito). It is also evident that incubation with SLN Mito-FA results in a stronger fluorescence inside the cell compared to their non-functionalized counterparts,

A
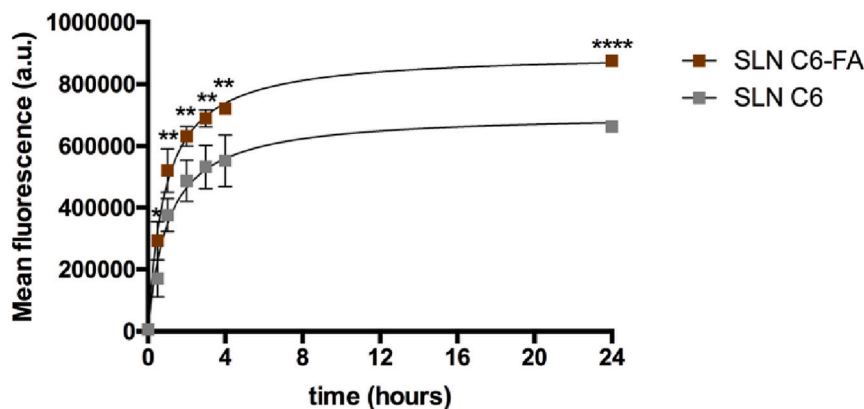
B

	V_{max}	k
SLN C6	704691 $\pm$ 32091	1.04 $\pm$ 0.17
SLN C6-FA	901008 $\pm$ 24190	0.88 $\pm$ 0.09

Fig. 5. Cellular uptake of C6-labelled SLN in MCF-7 cells using flow cytometry. (A) Time-dependent uptake of functionalized (SLN C6-FA) and non-functionalized (SLN C6) C6-labelled SLN for 24 h. Values represent mean $\pm$ SD; $n = 3$. Differences between groups were assessed using two-way ANOVA followed by Sidak post-hoc test. *$p < 0.05$, **$p < 0.01$, ****$p < 0.0001$ (B) Michaelis-Menten kinetics parameters for SLN C6 and SLN C6-FA.
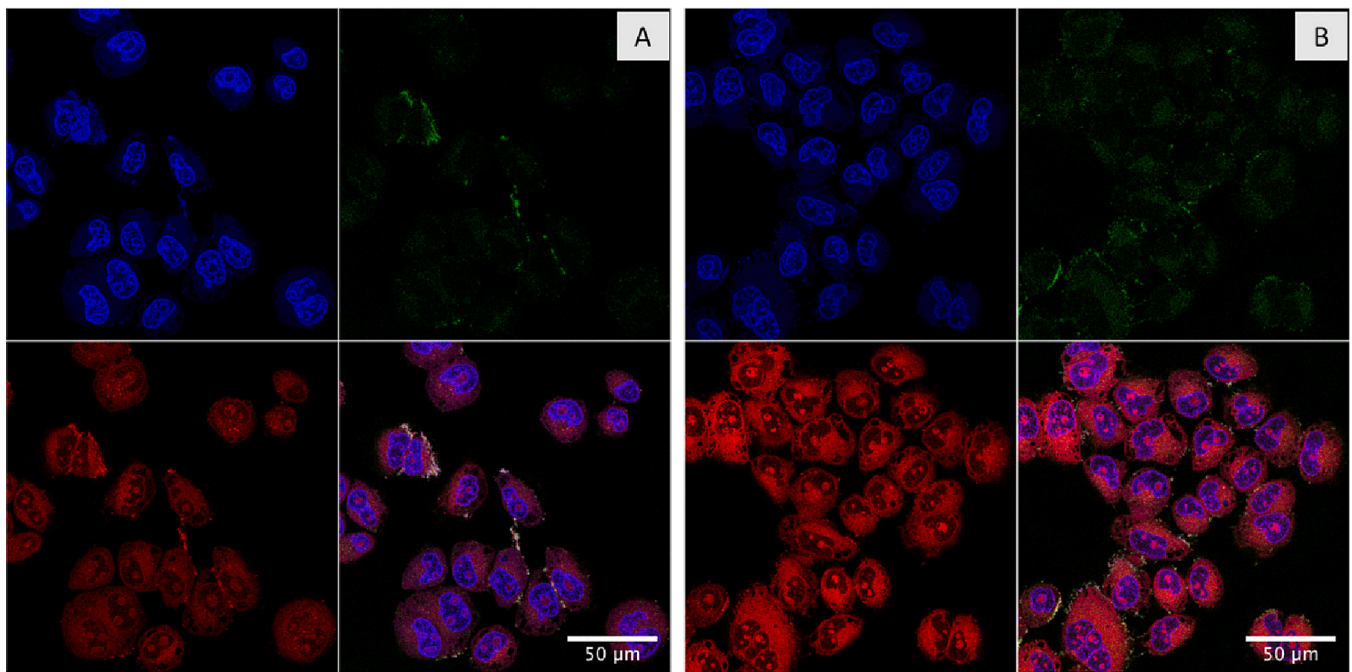
Fig. 6. CLSM images of SLN uptake in MCF-7 cells. Cellular uptake of non-functionalized (SLN Mito) (A) and functionalized SLN (SLN Mito-FA) (B) after incubation for 4 h. Blue channel: Hoechst 33342® (nucleus). Green channel: LysoTracker™ Green DND-26 (Lysosomes). Red channel: Mito.
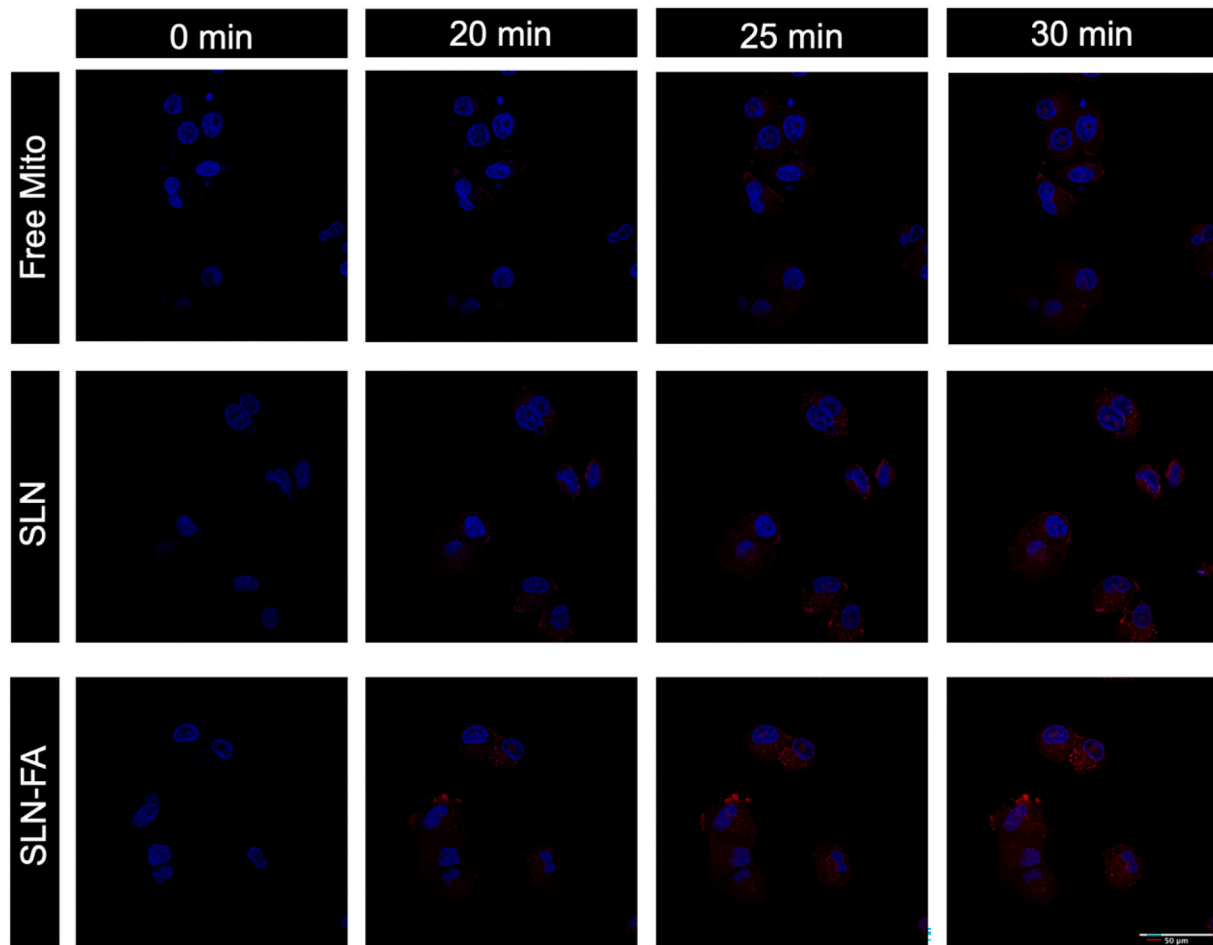

Fig. 7. Time-lapse CLSM of the MCF-7 cellular uptake of free Mito, SLN Mito and SLN Mito-FA. Cells were incubated under different conditions at 37 °C for 30 min in the confocal incubator chamber and images were acquired every 5 min. (A) CLSM images of uptake of free Mito, SLN Mito and SLN Mito-FA in MCF-7 cells for 30 min.

suggesting a quicker and higher internalization of the functionalized SLN, mediated by the FR overexpressed in MCF-7 cells [47]. After 24 h (Fig. S2), as expected, a much higher signal of the red channel was observed, with a translocation of Mito to the nucleus, which is the local of action of the drug, as denoted by the co-localization of the blue and red fluorescence. This effect can be attributed to a time-dependent cellular uptake and also to the gradual release of Mito over time as shown in Fig. 2B. Moreover, a higher accumulation of the SLN Mito-FA in the cytoplasm could also be observed, although less evident than at 4 h incubation, which may reflect saturation of the cellular uptake at 24 h. Additionally, a higher signal in the cell nucleus is also noticeable in the cells incubated with functionalized SLN, once again suggesting a higher internalization. Overall CLSM data corroborate the flow cytometry results, demonstrating a higher cellular uptake of the functionalized nanoparticles, compared to their non-functionalized counterparts, suggesting a successful active targeting strategy.

To study the dynamics of cellular uptake in real-time, time-lapse CLSM was performed (Fig. 7). MCF-7 cells were incubated with free Mito, SLN Mito and SLN Mito-FA for 30 min and images were recorded at pre-determined time points. As it can be observed in Fig. 7 nanoparticle uptake occurs approximately at 20 min of incubation. A higher red fluorescence intensity is observed following treatment with functionalized SLN for all the studied incubation times, pointing to the occurrence of a faster and higher cancer cell internalization of these nanoparticles. Interestingly, both nanoformulations led to an enhanced Mito uptake in comparison with incubation with the free drug. Similar facts have been reported in other studies for the Mito analog doxorubicin [48,49]. This fact can be related to the lipophilicity of SLN, which enhances the interaction with the cell membranes, thus improving drug intracellular delivery [48,50]. Moreover, free Mito and Mito-loaded SLN may be internalized through distinctive mechanisms. Free Mito internalization occurs mainly through passive [51] or flip-flop diffusion [52], being subjected to P-glycoprotein (P-gp)-mediated efflux [52]. In contrast, nanoparticles are generally internalized *via* endocytosis, which may improve intracellular drug delivery and evade P-gp-mediated drug efflux [49,53].

Overall these data support that FA functionalization resulted in a faster and higher cancer cell uptake for the first 30 min of incubation with the nanoparticles, demonstrating the efficacy of the functionalization.

3.6. Chemo and phototherapeutic combined effects

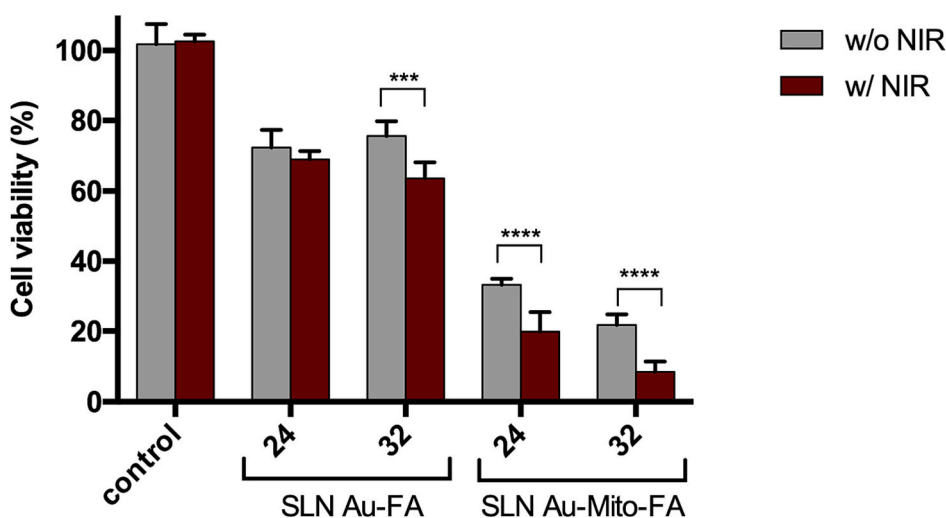After evaluating the cytocompatibility of the nanosystem and the targeting efficiency towards MCF-7 cells, the combined photo and chemotherapeutic effects of the nanoformulation were analyzed at two different concentrations of AuNRs (Fig. 8). Cells were incubated with the nanoformulations and after 4 h, exposed to NIR light for 5 min at a power density of 1.7 W cm^{-2}, which is in agreement with previous works for gold-based nanomaterials [54,55]. A control comprising cells treated with only DMEM-F12 exposed to NIR light was also included. As shown in Fig. 8, there were no differences between irradiated and non-irradiated control cells, demonstrating that NIR irradiation *per se*, did not induce any alterations in cancer cell viability. In contrast, NIR light induced a significant reduction in cancer cell viability after treatment with SLN Au-FA at the highest concentration tested (corresponding to 32 μg/mL of AuNRs), demonstrating the PTT effect of the nanosystem. Moreover, for Mito-loaded SLN, both concentrations tested were able to elicit a higher cancer cell death following exposure to NIR light. At the highest concentration tested (32 μg/mL of AuNRs and equivalent 10 μg/mL of Mito), cell viability decreased from 22 to 8 %, which can be attributed to the combined actions of PTT, chemotherapy and NIR-induced drug release.

4. Conclusion

In this work, novel multifunctional lipid nanoparticles co-loaded with mitoxantrone and gold nanorods were produced by combining PTT and chemotherapy to improve breast cancer treatment. Nanoparticles presented suitable physicochemical characteristics for intravenous injection and passive tumor accumulation. Additionally, an active targeting strategy was implemented by functionalizing the nanoparticles' surface with a folic acid conjugate. A temperature increase up to 20 °C was mediated by the nanoformulation upon near-infrared laser irradiation, demonstrating its suitability for PTT applications. Additionally, an increased drug release occurred following light exposure for 5 min, suggesting that the temperature variation was enough to destabilize the lipid matrix structure. Moreover, nanoparticles did not induce hemolysis and were well tolerated by healthy cells. The functionalization was found to be effective, leading to higher nanoparticle accumulation in MCF-7 cells, which was shown by confocal microscopy and flow cytometry studies. Finally, the chemo-phototherapeutic effect of the nanoformulation were evaluated in MCF-7 cells. Laser irradiation induced a significant reduction in cancer cell viability following incubation with drug-loaded and unloaded nanoparticles demonstrating the phototherapeutic effect of the nanosystem. Furthermore, a demarked increase in cancer cell death was obtained due to the combined effects of chemotherapy, NIR-induced drug release and PTT. Taking into consideration the advantages of using lipid nanoparticles, mainly their low-cost manufacture and easy

Fig. 8. Photo and chemotherapeutic effects in MCF-7 cells. Phototherapeutic and combined PTT-chemotherapy effects of the nanoparticles were studied in MCF-7 cells upon NIR laser irradiation (808 nm, 1.7 W cm^{-2}) for 5 min. Cells were treated for 24 h. Data are represented as mean ± SD ($n = 5$). Control w/o NIR represents cells solely incubated with DMEM F-12. Control w/ NIR corresponds to cells only incubated with DMEM F-12 and irradiated with NIR light. Differences between conditions were determined using two-way ANOVA followed by Sidak post-hoc test ***$p < 0.001$, ****$p < 0.0001$.

scale-up, we believe that this approach may contribute to the development of a viable multimodal therapeutic modality in the near future. Only one study has reported the development of lipid nanoparticles for the combination of chemotherapy and PTT using gold nanostructures. Zheng et al. developed a nanoformulation based on nanostructured lipid carriers *co*-loaded with doxorubicin and polyhedral gold nanoparticles aiming to combine chemotherapy, PTT and drug release. The authors could achieve a demarked reduction in cancer cell viability from approximately 20 to 10 % at a concentration of 20 µg/mL of doxorubicin and 500 µg/mL of NLC. Nevertheless, a high laser dose was used (20 W cm^{-2}) with an irradiation time of 10 min [24]. In our work, similar results were obtained using a lower laser power (1.7 W cm^{-2}) and only 5 min of irradiation. Overall these data suggest that the developed lipid nanosystem combining active cancer cell targeting, PTT, light-induced drug release, and chemotherapy represents a cost-effective approach for the multimodal therapy of breast cancer. Future work will be performed using an *in vivo* mice model of breast cancer to evaluate the biodistribution, bioaccumulation, and therapeutic efficacy of this nanoformulation.

CRediT authorship contribution statement

Andreia Granja: Conceptualization, Investigation, Data curation, Formal analysis, Writing – original draft. **Rita Lima-Sousa:** Investigation, Formal analysis, Writing – review & editing. **Cátia G. Alves:** Investigation, Formal analysis, Writing – review & editing. **Duarte de Melo-Diogo:** Supervision, Writing – review & editing. **Cláudia Nunes:** Investigation, Writing – review & editing. **Célia T. Sousa:** Supervision, Formal analysis, Writing – review & editing. **Ilídio J. Correia:** Resources, Supervision, Writing – review & editing. **Salette Reis:** Conceptualization, Resources, Supervision, Writing – review & editing.

Declaration of competing interest

The authors declare that they have no known competing financial interests or personal relationships that could have appeared to influence the work reported in this paper.

Data availability

Data will be made available on request.

Appendix A. Supplementary data

Supplementary data to this article can be found online at https://doi.org/10.1016/j.bioadv.2023.213443.

References

[1] H. Sung, J. Ferlay, R.L. Siegel, M. Laversanne, I. Soerjomataram, A. Jemal, F. Bray, CA Cancer J. Clin. 71 (2021) 209–249.
[2] K. Polyak, J. Clin. Invest. 121 (2011) 3786–3788.
[3] P.H. Tan, I. Ellis, K. Allison, E. Brogi, S.B. Fox, S. Lakhani, A.J. Lazar, E.A. Morris, A. Sahin, R. Salgado, Histopathology 77 (2020) 181–185.
[4] X. Bai, J. Ni, J. Beretov, P. Graham, Y. Li, Cancer Treat. Rev. 69 (2018) 152–163.
[5] J. Lee, J.-C. Kim, Colloids Surf. A Physicochem. Eng. Asp. 484 (2015) 441–448.
[6] A. Granja, M. Pinheiro, C.T. Sousa, S. Reis, Biochem. Pharmacol. 190 (2021) 114639–114663.
[7] N.S. Abadeer, C.J. Murphy, J. Phys. Chem. C 120 (2016) 4691–4716.
[8] P. Manivasagan, S. Bharathiraja, M.Santha Moorthy, S. Mondal, T.P. Nguyen, H. Kim, T.T.V. Phan, K.D. Lee, J. Oh, Polymers 10 (2018) 232. Basel.
[9] W. Xu, J. Qian, G. Hou, Y. Wang, J. Wang, T. Sun, L. Ji, A. Suo, Y. Yao, Acta Biomater. 82 (2018) 171–183.
[10] V.D. Nguyen, H.-K. Min, D.-H. Kim, C.-S. Kim, J. Han, J.-O. Park, E. Choi, ACS Appl. Mater. Interfaces 12 (9) (2020) 10130–10141.
[11] Y. Xing, J. Zhang, F. Chen, J. Liu, K. Cai, Nanoscale 9 (2017) 8781–8790.
[12] Y. Peng, J. Nie, W. Cheng, G. Liu, D. Zhu, L. Zhang, C. Liang, L. Mei, L. Huang, X. Zeng, Biomater.Sci. 6 (2018) 1084–1098.
[13] W. Fan, B. Yung, P. Huang, X. Chen, Chem. Rev. 117 (2017) 13566–13638.
[14] P.I. Siafaka, N. Üstündağ Okur, E. Karavas, D.N. Bikiaris, Int. J. Mol. Sci. 17 (2016) 1440.
[15] Y. Li, D. He, J. Tu, R. Wang, C. Zu, Y. Chen, W. Yang, D. Shi, T.J. Webster, Y. Shen, Nanoscale 10 (2018) 8628–8641.
[16] V.D. Nguyen, H.K. Min, C.S. Kim, J. Han, J.O. Park, E. Choi, Colloids Surf. B Biointerfaces 173 (2019) 539–548.
[17] T. Hashimoto, E. Yuba, A. Harada, K. Kono, J. Mater. Chem. B 8 (2020) 2826–2833.
[18] J. Wu, Y. Liu, Y. Tang, S. Wang, C. Wang, Y. Li, X. Su, J. Tian, Y. Tian, J. Pan, Y. Su, H. Zhu, Z. Teng, G. Lu, ACS Appl. Mater. Interfaces 8 (2016) 17927–17935.
[19] A.S. Monem, N. Elbialy, N. Mohamed, Int. J. Pharm. 470 (2014) 1–7.
[20] D. Encinas-Basurto, J. Ibarra, J. Juarez, A. Pardo, S. Barbosa, P. Taboada, M. A. Valdez, Mater. Sci. Eng. C 91 (2018) 669–678.
[21] W.M. Darwish, A.S. Abdoon, M.S. Shata, M. Elmansy, React. Funct. Polym. 151 (2020), 104575.
[22] J. Albuquerque, C.C. Moura, B. Sarmento, S. Reis, Molecules 20 (2015) 11103–11118. Basel, Switzerland.
[23] Y.S. Ong, M. Bañobre-López, S.A.C. Lima, S. Reis, Mater. Sci. Eng. C 116 (2020), 111255.
[24] S. Zheng, V.D. Nguyen, S.Y. Song, J. Han, J.O. Park, Nanotechnology 28 (2017), 435102.
[25] A. Granja, R. Lima-Sousa, C.G. Alves, D. de Melo-Diogo, M. Pinheiro, C.T. Sousa, I. J. Correia, S. Reis, Int. J. Pharm. 607 (2021) 121044–121047.
[26] P. Varadwaj, K. Misra, A. Sharma, R. Kumar, Electron.J.Biol. 6 (2010) 36–42.
[27] T.S. Herman, Cancer Treat. Rep. 67 (1983) 1019.
[28] Y.G. Assaraf, C.P. Leamon, J.A. Reddy, Drug Resist. Updat. 17 (2014) 89–95.
[29] J. Lopes-de-Araújo, A.R. Neves, V.M. Gouveia, C.C. Moura, C. Nunes, S. Reis, Pharm. Res. 33 (2016) 301–314.
[30] C.G. Alves, D. de Melo-Diogo, R. Lima-Sousa, I.J. Correia, Int. J. Pharm. 582 (2020) 119346.
[31] R. Lima-Sousa, D. de Melo-Diogo, C.G. Alves, C.S. Cabral, S.P. Miguel, A. G. Mendonça, I.J. Correia, Mater. Sci. Eng. C 117 (2020), 111294.
[32] M.I. Silva, A.I. Barbosa, S.A. Costa Lima, P. Costa, T. Torres, S. Reis, Nanomaterials 10 (2020) 986.
[33] R. Singh, J.W. Lillard Jr., Exp. Mol. Pathol. 86 (2009) 215–223.
[34] S. Wang, Z. Liu, Y. Tong, Y. Zhai, X. Zhao, X. Yue, Y. Qiao, Y. Liu, Y. Yin, R. Xi, J. Control. Release 330 (2021) 483–492.
[35] M. Danaei, M. Dehghankhold, S. Ataei, F. Hasanzadeh Davarani, R. Javanmard, A. Dokhani, S. Khorasani, M. Mozafari, Pharmaceutics 10 (2018) 57.
[36] M.A. Brown, A. Goel, Z. Abbas, Angew. Chem. 128 (2016) 3854–3858.
[37] K. Xiao, Y. Li, J. Luo, J.S. Lee, W. Xiao, A.M. Gonik, R.G. Agarwal, K.S. Lam, Biomaterials 32 (2011) 3435–3446.
[38] S.C. Freitas, J.H. Belo, A. Granja, M. Canhota, A.S. Silva, S. Reis, H. Crespo, J. P. Araújo, C.T. Sousa, Adv. Mater. Interfaces (2023) 2202214.
[39] A. Espinosa, J. Kolosnjaj-Tabi, A. Abou-Hassan, A. Plan Sangnier, A. Curcio, A. K. Silva, R. Di Corato, S. Neveu, T. Pellegrino, L.M. Liz-Marzán, Adv. Funct. Mater. 28 (2018), 1803660.
[40] X. Liu, B. Li, F. Fu, K. Xu, R. Zou, Q. Wang, B. Zhang, Z. Chen, J. Hu, Dalton Trans. 43 (2014) 11709–11715.
[41] Z. Mei, D. Gao, D. Hu, H. Zhou, T. Ma, L. Huang, X. Liu, R. Zheng, H. Zheng, P. Zhao, Biomaterials 251 (2020), 120092.
[42] U. Ruktanonchai, U. Sakulkhu, P. Bejrapha, P. Opanasopit, N. Bunyapraphatsara, V. Junyaprasert, S. Puttipipatkhachorn, J. Microencapsul. 26 (2009) 614–626.
[43] M. Schubert, C. Müller-Goymann, Eur. J. Pharm. Biopharm. 61 (2005) 77–86.
[44] X.-Y. Ying, D. Cui, L. Yu, Y.-Z. Du, Carbohydr. Polym. 84 (2011) 1357–1364.
[45] S. Doktorovova, E.B. Souto, A.M. Silva, Eur. J. Pharm. Biopharm. 87 (2014) 1–18.

[46] R. Faria, A. Sousa, A.R. Neves, J.A. Queiroz, D. Costa, J. Mol. Liq. 292 (2019), 111391.

[47] J. Soleymani, M. Hasanzadeh, M.H. Somi, N. Shadjou, A. Jouyban, Biosens. Bioelectron. 115 (2018) 61–69.

[48] S.V. Mussi, R.C. Silva, M.C. de Oliveira, C.M. Lucci, R.B. de Azevedo, L.A. M. Ferreira, Eur. J. Pharm. Sci. 48 (2013) 282–290.

[49] H.S. Yoo, T.G. Park, J. Control. Release 96 (2004) 273–283.

[50] H.L. Wong, A.M. Rauth, R. Bendayan, J.L. Manias, M. Ramaswamy, Z. Liu, S. Z. Erhan, X.Y. Wu, Pharm. Res. 23 (2006) 1574–1585.

[51] C.P. Burns, B.N. Haugstad, J.A. North, Biochem. Pharmacol. 36 (1987) 857–860.

[52] R. Regev, D. Yeheskely-Hayon, H. Katzir, G.D. Eytan, Biochem. Pharmacol. 70 (2005) 161–169.

[53] S. Shahabi, S. Döscher, T. Bollhorst, L. Treccani, M. Maas, R. Dringen, K. Rezwan, ACS Appl. Mater. Interfaces 7 (2015) 26880–26891.

[54] X. Liu, Q. Su, H. Song, X. Shi, Y. Zhang, C. Zhang, P. Huang, A. Dong, D. Kong, W. Wang, Biomaterials 275 (2021), 120921.

[55] C. Xu, T. Zhang, G. Lu, K. Chen, J. Tao, Y. Zhang, Z. Teng, B. Yang, Biomater.Sci. 8 (2020) 3310–3319.